

Semi-transparent and stable $\text{In}_2\text{S}_3/\text{CdTe}$ heterojunction photoanodes for unbiased photoelectrochemical water splitting

Received: 28 October 2024

Accepted: 26 May 2025

Published online: 02 June 2025



Yuan Cai^{1,2}, Shujie Wang^{1,2,3,4,5}, Bin Liu^{1,2}, Gong Zhang¹, Hui Gao¹, Yuting Tong^{1,2}, Qingfeng Chang^{1,2}, Peng Zhang^{1,2,3,4,5}, Tuo Wang^{1,2,3,4,5} ✉ & Jinlong Gong^{1,2,6,7} ✉

The development of low-cost, high-performance, and stable photoanodes is essential for solar-driven photoelectrochemical energy conversion. In_2S_3 , an n-type semi-transparent semiconductor (~2.0 eV), is particularly well-suited as a photoanode in PEC tandem devices. However, the Schottky barrier at the $\text{In}_2\text{S}_3/\text{FTO}$ interface as well as the inherent defects in In_2S_3 suppress charge extraction. This paper describes the design of a semi-transparent photoanode aimed at enhancing carrier mobility for unassisted water splitting. We incorporate a semi-transparent Ag layer at the $\text{FTO}/\text{In}_2\text{S}_3$ interface to establish an ohmic contact, effectively resolving the conflict between light shielding of metal and the electron collection barrier from In_2S_3 to FTO. Additionally, the $\text{In}_2\text{S}_3/\text{CdTe}$ p-n heterojunction forms an effective built-in electric field, which serves as a strong driving force for the separation and migration of photo-generated charges. The $\text{Ag}/\text{Ag};\text{In}_2\text{S}_3/\text{In}_2\text{S}_3/\text{CdTe}/\text{NiO}_x/\text{TiO}_2/\text{Ni}$ semi-transparent photoanode exhibits a photocurrent density of $12.2 \text{ mA}/\text{cm}^2$ at 1.23 V vs. reversible hydrogen electrode, with stable operation for 60 h. Pairing a back-illuminated Si photocathode with an $\text{In}_2\text{S}_3/\text{CdTe}$ semi-transparent photoanode enables a solar-to-hydrogen conversion efficiency of 5.10%.

Photoelectrochemical (PEC) water splitting has gained significant attention as a promising method to generate sustainable and clean hydrogen energy^{1–4}. However, compared to the proton reduction reaction, the kinetics of the water oxidation reaction is slow. This reaction involves a complex multi-step process of proton-coupled electron transfer, necessitating large overpotentials to drive the reaction^{5–7}. Thus, the development of highly active photoanodes is crucial to achieving high-efficiency and large-scale solar-to-chemical energy conversion systems based on PEC water splitting technology. To date, a variety of metal oxides, nitrides, and oxynitrides have been

developed to fabricate photoanodes, including WO_3 , BiVO_4 , Fe_2O_3 , TaON , and Ta_3N_5 ^{7–13}. Nonetheless, the current focus of research predominantly lies in the study of individual photoanodes or photocathodes, making it challenging to identify semiconductor materials that can effectively match and generate efficient and stable bias-free PEC tandem devices. Thus, the solar-to-hydrogen (STH) conversion efficiency in standalone unbiased PEC tandem devices is still limited to 5%¹⁴.

Recent studies have shown that STH efficiency of PEC water splitting can be improved by over 20% in photoanode–photocathode

¹School of Chemical Engineering & Technology, Key Laboratory for Green Chemical Technology of Ministry of Education, Tianjin University; Collaborative Innovation Center for Chemical Science & Engineering, Tianjin, China. ²International Joint Laboratory of Low-carbon Chemical Engineering of Ministry of Education, Tianjin, China. ³Haihe Laboratory of Sustainable Chemical Transformations, Tianjin, China. ⁴Joint School of National University of Singapore and Tianjin University, International Campus of Tianjin University, Binhai New City, Fuzhou, China. ⁵National Industry-Education Platform of Energy Storage, Tianjin, China. ⁶State Key Laboratory of Synthetic Biology, Tianjin University, Tianjin, China. ⁷Tianjin Normal University, Tianjin, China.

✉ e-mail: wangtuo@tju.edu.cn; jlgon@tju.edu.cn

tandem cell configuration by pairing first and second absorber semiconductors with bandgaps of ~ 1.8 eV and 1.2 eV, respectively¹⁵. For small bandgap semiconductors, silicon (Si) is a suitable choice due to its narrow bandgap (1.12 eV), abundant earth resources, and mature production technology¹⁶. Photoanode semiconductors feature a wide bandgap, which facilitates the efficient absorption of high-energy photons, such as ultraviolet and short-wavelength light. However, their capacity to absorb longer-wavelength light remains relatively limited. To fully exploit the entire spectral range of sunlight, the wide-bandgap photoanode must possess semi-transparent properties, allowing long-wavelength light that is not absorbed by the wide-bandgap material to pass through the photoanode and subsequently irradiate the photocathode. If the photoanode lacks transparency, some of the light energy will be absorbed and converted into heat within the anode, resulting in energy losses. The semi-transparent photoanode enables more light to pass through and reach the photocathode, thereby reducing ineffective energy consumption and enhancing the STH efficiency of the independent unbiased PEC tandem device.

The widely studied semi-transparent photoelectrodes for water oxidation include TiO_2 ($3.0\text{--}3.2$ eV)^{17,18}, WO_3 ($2.5\text{--}2.8$ eV)^{19,20}, Fe_2O_3 ($2.0\text{--}2.2$ eV)²¹, and BiVO_4 (2.4 eV)^{22,23}. However, these semi-transparent materials exhibit inherent limitations. For example, TiO_2 , WO_3 , and BiVO_4 have relatively wide bandgaps, which restrict their light absorption range. In contrast, $\alpha\text{-Fe}_2\text{O}_3$ features a narrower bandgap but suffers from a short carrier lifetime and pronounced surface charge recombination, limiting its photoelectrochemical performance²¹. To enhance the performance of semi-transparent photoanodes, researchers have developed structures such as $\text{BiVO}_4/\alpha\text{-Fe}_2\text{O}_3$ ²⁴ and $\text{TiO}_2/\text{BiVO}_4$ ²⁵, which effectively extend the spectral range of light harvesting within the solar spectrum. Meanwhile, researchers have introduced transparent carrier transport layers, such as WO_3 and CuSCN , into semi-transparent photoanodes to improve charge transport efficiency and suppress carrier recombination^{26–29}. However, the development of semi-transparent photoanodes with an optimal bandgap that can simultaneously deliver high photocurrent density and effectively pair with photocathodes remains a critical challenge for achieving high-efficiency unbiased photoelectrochemical water splitting.

Among various wide bandgap semiconductors, metal sulfides have attracted much attention for pairing with Si, motivated by its suitable bandgap. Indium sulfide (In_2S_3) is a semi-transparent n-type semiconductor with a defective spinel structure that has been widely used in many fields, such as photocatalysts, photodetectors, and solar cells^{30–32}. $\beta\text{-In}_2\text{S}_3$ is a stable phase with a bandgap of $2.0\text{--}2.3$ eV, perfectly matching the bandgap requirement for the photoanode in high-performance PEC tandem devices³³. Moreover, $\beta\text{-In}_2\text{S}_3$ exhibits several compelling advantages, such as a large light absorption coefficient, long hole diffusion lengths, offering broad applications under visible light irradiation^{34,35}. Unfortunately, the highest photocurrent density achieved for In_2S_3 photoanodes is only ~ 8.43 mA/cm² in $0.5\text{ M Na}_2\text{SO}_4$ aqueous solution³⁶.

One of the primary challenges limiting the performance of In_2S_3 photoelectrodes is the difficulty in forming ohmic contacts between In_2S_3 and fluorine-doped tin oxide (FTO) substrates, which impedes carrier transport. In the existing literature about In_2S_3 photoanodes, many studies focus on enhancing device performance through heterojunction construction, with limited attention devoted to establishing ohmic contact between In_2S_3 and FTO^{33,37–40}. Although it is easy to form effective ohmic contacts in metal/semiconductor junctions, the incorporation of metal materials into photoanode devices can substantially reduce the overall transparency of these devices, which limits their applicability as photoanodes in tandem cells. To manufacture high-performance In_2S_3 photoanode devices, it is essential to achieve both robust ohmic contact and substantial transparency between the conductive substrate and the semiconductor layer,

thereby ensuring optimal current density injection through the contact.

Another limiting factor of In_2S_3 photoelectrodes is the severe carrier recombination and inefficient carrier migration. Heterojunction photoelectrodes, by establishing a built-in electric field between two semiconductors, facilitate the effective separation and transfer of charges, thereby enhancing photocurrent generation^{41–43}. Cadmium telluride (CdTe), a p-type semiconductor with a direct bandgap of ~ 1.45 eV, emerges as a suitable photo-absorber for PEC water splitting applications^{44–47}. This material can absorb up to 850 nm light and can provide a photocurrent density up to 29.0 mA/cm² (see ref. 48). Researchers demonstrated that an n-type CdTe single-crystal wafer-based photoanode surface modified with TiO_2 and Ni layers shows stable water oxidation activity⁴⁷. Furthermore, Hu et al. developed a multilayer $\text{CdS}/\text{CdTe}/\text{TiO}_2/\text{Ni}/\text{NiO}_x$ photoanode that achieved a photocurrent density of 24.5 mA/cm² and demonstrated 100 h stability for water oxidation under light-on/light-off cycles⁴⁹. However, the inherent opacity of CdTe limits its suitability for use in transparent photoanodes. It is worth noting that while many studies focus on constructing p–n junction to improve the driving force of carrier separation, there is often less emphasis on matching the bandgap of p–n junction and the contact between semiconductor material and FTO (either ohmic or Schottky contact), as well as the selection of transport layer (electron transport layer, hole transport layer). At this point, the presence of high defect density at the interface, caused by complex lattice mismatches in two semiconductors, leads to interface-induced recombination, thereby reducing device efficiency. Therefore, constructing a p–n junction in a photoanode requires comprehensive consideration of band alignment and semiconductor material transparency⁵⁰.

This work describes the design and fabrication of a semi-transparent $\text{Ag}/\text{Ag}:\text{In}_2\text{S}_3/\text{In}_2\text{S}_3/\text{CdTe}/\text{NiO}_x/\text{TiO}_2/\text{Ni}$ photoanode with high charge separation efficiency, featuring the formation of both ohmic contacts and p–n junctions for the tandem configuration. A semi-transparent Ag layer, featured by a low work function, can form ohmic contact with In_2S_3 , facilitating the directional migration of photogenerated electrons. A bandgap matched $\text{In}_2\text{S}_3/\text{CdTe}$ p–n junction is constructed to form an internal electric field at the contact interface, which accelerates the accumulation of electrons and holes in the conduction band of n- In_2S_3 and valence band of p- CdTe , thus enhancing charge separation efficiency. The strategic deposition of Ag and NiO_x on the illuminated and back sides of p–n junction improved the transport efficiency of photogenerated electrons and holes, effectively inhibiting the recombination of electron–hole pairs for prolonged the carrier life⁵¹. As a result, the photocurrent density of the photoanode with an $\text{In}_2\text{S}_3/\text{CdTe}$ p–n junction increased from 6.1 mA/cm² to 12.2 mA/cm² at 1.23 V vs. reversible hydrogen electrode (RHE), compared to the photoanode without a p–n junction, and an applied bias photon-to-current efficiency (ABPE) of $\sim 3.03\%$ at 0.85 V vs. RHE with a long-term operation for at least 60 h. In addition, a standalone unbiased PEC tandem cell is demonstrated by using this newly developed semi-transparent photoanode and a back-illuminated silicon photocathode, which achieves a 5.10% STH efficiency. The current density and stability of the obtained In_2S_3 photoanode device surpass those reported previously, demonstrating that the ohmic contact and p–n junction structure enhance the photogenerated current density, while the dense ALD-deposited TiO_2 protective layer contributes to the improved stability of the photoanode device.

Results

Construction of $\text{In}_2\text{S}_3/\text{CdTe}$ photoanodes for the OER

To improve the photocurrent density of In_2S_3 photoanodes, Ag, CdTe , and NiO_x layers were designed and fabricated using magnetron sputtering. The p–n structure is utilized to build an internal electric field, improving charge separation efficiency, while the ohmic contact and

hole transport layer are employed to enhance the directional transfer efficiency of photogenerated electrons and holes^{52–55}. The Ag layer was first fabricated using direct current (DC) sputtering, followed by the sequential deposition of In_2S_3 , CdTe, and NiO_x films using radio frequency (RF) sputtering. Under thermal annealing, Ag atoms are gradient-doped into the In_2S_3 layer, which introduces additional free electrons, increases the carrier density, and consequently enhances the electrical conductivity of In_2S_3 . A 10-nm-thick TiO_2 protective layer was deposited on the surface of the NiO_x layer using atomic layer deposition (ALD)^{56–59}, effectively suppressing the corrosion of the photoanode during the water oxidation process^{60–62}. Due to the presence of defect states (0–2 eV versus to the conduction band edge) in the TiO_2 film, hole conduction exhibited negligible voltage loss, enabling efficient hole transport to the Ni catalyst layer⁶⁰. Finally, a Ni catalyst layer was deposited onto the TiO_2 layer to fabricate a semi-transparent In_2S_3 -based photoanode with the $\text{Ag}/\text{Ag}:\text{In}_2\text{S}_3/\text{In}_2\text{S}_3/\text{CdTe}/\text{NiO}_x/\text{TiO}_2/\text{Ni}$ structure (Fig. 1a and Supplementary Fig. 1). The transmittance of the FTO/Ag (300 °C) side is approximately 70%, while the transmittance of the FTO/CdTe/ $\text{NiO}_x/\text{TiO}_2/\text{Ni}$ device on the other side ranges between 40 and 50% (Supplementary Fig. 2). Therefore, illumination from the FTO/Ag (300 °C) side (back illumination) allows a larger amount of light to pass through and reach the In_2S_3 light absorption layer. This back-illumination strategy effectively leverages the spectral matching between wide-bandgap and narrow-bandgap semiconductors, thereby enhancing the overall device performance. The entire FTO glass device (yellow area) is exposed to sunlight, while the region within the white box represents the working area of the photoanode (Supplementary Fig. 3b). Image J software is used to accurately measure the effective working area of the device, which is determined to be 1.419 cm^2 (Supplementary Fig. 3a).

Establishing effective ohmic contacts between FTO and In_2S_3 poses a significant challenge, hindering the efficient transfer of photogenerated electrons in semi-transparent In_2S_3 photoanodes and leading to increased carrier recombination. Adding a work function

tuning layer at the FTO/ In_2S_3 interface may solve this problem. The work function of Ag is 4.50 eV, which is lower than that of In_2S_3 (4.75 eV), facilitating the formation of a good ohmic contact between Ag and In_2S_3 , allowing unimpeded transfer of majority carriers^{63,64}. However, the opacity of Ag does not meet the requirements for transparent photoanodes. Therefore, by adjusting the sputtering time and combining with the transmittance requirements of the photoanode, the optimal thickness of Ag was determined to be 10 nm (Supplementary Fig. 4 and Supplementary Table 1). Meanwhile, the In_2S_3 thin films obtained via sputtering demonstrate high transmittance, fulfilling the requirement for semi-transparent photoanodes (Supplementary Fig. 5 and Supplementary Table 2). To achieve a semi-transparent photoelectrode device, the thickness and light transmittance of CdTe are optimized. (Supplementary Fig. 6b, c and Supplementary Table 3). As the sputtering time increases from 15 to 240 s, the CdTe thin film gradually changes from a semi-transparent light brown to an opaque black film (Supplementary Fig. 6a). When the sputtering time becomes 30 s, the thickness of the CdTe thin film is ~76.47 nm, which not only meets the requirements for a semi-transparent photoanode but also allows for the construction of a p–n junction with the In_2S_3 film.

To study the composition and chemical state of the thin films obtained by the magnetron sputtering method, Ag, In_2S_3 , and CdTe films were analyzed using X-ray photoelectron spectroscopy (XPS). All spectra were calibrated against the C 1s signal at 284.8 eV. The presence of O element is attributed to the ambient exposure of the sample surface during the annealing process (Supplementary Fig. 7). Sputtering 15 s of Ag onto FTO for XPS analysis revealed two peaks at 368.6 eV and 374.6 eV, which correspond to the reported binding energies of $\text{Ag } 3d_{3/2}$ and $\text{Ag } 3d_{5/2}$, respectively (Supplementary Fig. 8)⁶⁵. This confirms the successful deposition of an Ag layer on FTO. The peaks at 444.5 eV and 452.0 eV corresponded to the $\text{In } 3d_{5/2}$ and $\text{In } 3d_{3/2}$ states of In^{3+} , respectively (Supplementary Fig. 9a). The presence of two peaks at 161.4 eV and 162.6 eV is consistent with the reported

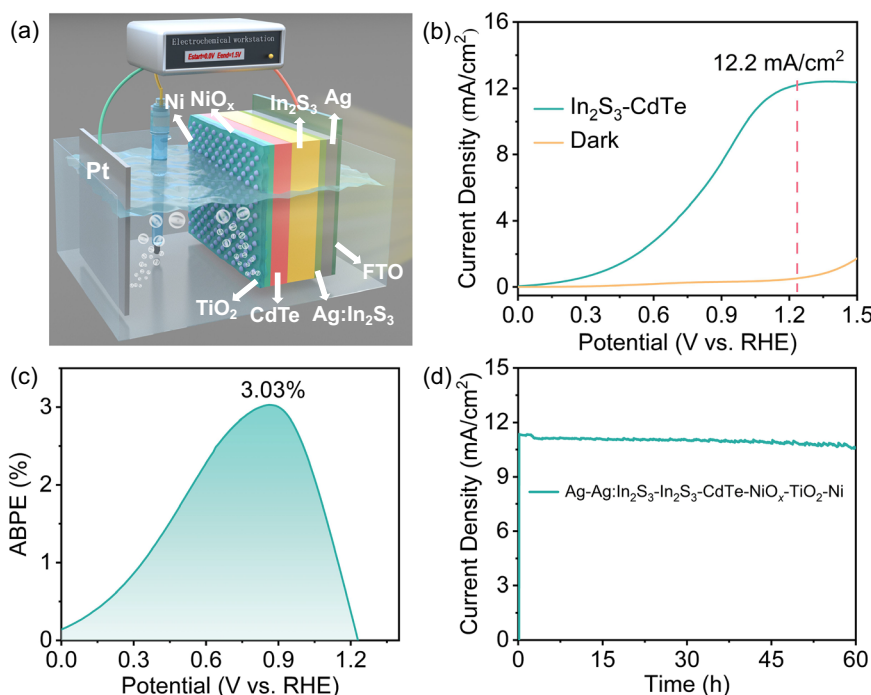


Fig. 1 | The configuration and PEC performances of $\text{In}_2\text{S}_3/\text{CdTe}$ photoanode. **a** Schematic illustration of the transparent $\text{In}_2\text{S}_3/\text{CdTe}$ photoanode (the light is incident from the FTO/Ag (300 °C) side for back illumination). **b** J–V plots under simulated AM 1.5 G illumination, **c** ABPE, and **d** stability test of the $\text{Ag}/\text{Ag}:\text{In}_2\text{S}_3/$

$\text{In}_2\text{S}_3/\text{CdTe}/\text{NiO}_x/\text{TiO}_2/\text{Ni}$ photoanode. All measurements were conducted in a 1.0 M NaOH electrolyte. The experiments are conducted without iR compensation. Source data are provided in the Source Data file.

binding energies for the S $2p_{3/2}$ and S $2p_{1/2}$ states of In_2S_3 (Supplementary Fig. 9b)^{33,66}. The spectrum shows the characteristic peaks of the Cd element appearing at 404.8 eV ($3d_{5/2}$) and 411.5 eV ($3d_{3/2}$), which approximate the energy levels of CdTe (Supplementary Fig. 9c)^{67,68}. The Te $3d$ spectrum exhibits two prominent peaks at 575.8 eV (Te $3d_{3/2}$) and 586.2 eV (Te $5d_{5/2}$) (Supplementary Fig. 9d)⁶⁹. These results confirm the successful fabrication of In_2S_3 and CdTe films on the FTO substrates.

To investigate the occurrence of element doping in $\text{Ag}/\text{In}_2\text{S}_3$ during annealing, deep-profile XPS scanning was conducted on the annealed FTO/ $\text{Ag}/\text{In}_2\text{S}_3$ samples. High-resolution XPS spectra recorded after each etching cycle reveal the evolution in the Ag $3d$, and In $3d$ spectra as a function of depth for fully dense brushes (Supplementary Fig. 10). When the depth-profiling times were 40, 90, and 140 s, no characteristic peaks of Ag were observed, indicating that the Ag element does not diffuse into the In_2S_3 layer within this thickness range after annealing. When the depth-profiling times were 240, 340, 440, and 540 s, the characteristic peaks of Ag gradually increased, indicating that Ag is gradient-doped into the In_2S_3 layer within a certain depth range. The intensity of the characteristic peaks of In remained unchanged throughout the depth-profiling experiment, indicating that the elemental distribution of In_2S_3 after annealing is uniform in the vertical direction.

To examine the differences in the crystal plane structure of thin films obtained via magnetron sputtering, the elemental distribution and crystal plane structure of In_2S_3 and CdTe thin films were analyzed using transmission electron microscopy (TEM). The In_2S_3 and CdTe layers deposited on the glass surface were mechanically peeled off in the form of powder for TEM analysis. The high-resolution transmission electron microscopy (HRTEM) image shows a lattice spacing of 0.268 nm, corresponding to the (011) plane of In_2S_3 , indicating preferential growth along the [011] direction (Supplementary Fig. 11a)³⁸. The presence of well-resolved lattice surfaces indicates that CdTe is highly crystallized and exhibits a wurtzite crystal structure, with a lattice plane distance of 0.374 nm corresponding to the (002) plane of CdTe (Supplementary Fig. 11c)⁷⁰. All elements were evenly distributed, as shown by EDS on TEM, which is consistent with SEM result (Supplementary Fig. 12b, c, e, f).

To clarify the effect of constructing a p–n junction on the performance of the In_2S_3 photoanode, the PEC performances of $\text{Ag}/\text{Ag}:\text{In}_2\text{S}_3/\text{In}_2\text{S}_3/\text{NiO}_x/\text{TiO}_2/\text{Ni}$ and $\text{Ag}/\text{Ag}:\text{In}_2\text{S}_3/\text{In}_2\text{S}_3/\text{CdTe}/\text{NiO}_x/\text{TiO}_2/\text{Ni}$ photoanodes were examined by linear sweep voltammetry (LSV) under AM 1.5 G illumination (100 mW cm^{-2}) in 1 M NaOH aqueous solution (Supplementary Fig. 13). The $\text{Ag}/\text{Ag}:\text{In}_2\text{S}_3/\text{In}_2\text{S}_3/\text{NiO}_x/\text{TiO}_2/\text{Ni}$ photoanode exhibits a relatively low photocurrent density of 6.1 mA cm^{-2} at 1.23 V *vs.* RHE (Supplementary Fig. 14a). Upon the deposition of CdTe on In_2S_3 , the photocurrent density increased remarkably to 12.2 mA cm^{-2} at the same potential (Fig. 1b). The incident photon-to-current efficiency (IPCE) of the device was measured at a potential of 1.23 V *vs.* RHE. By integrating the measured IPCE over the standard AM 1.5 G spectrum (ASTM G173-03), the integrated current densities of the In_2S_3 photoanode and $\text{In}_2\text{S}_3/\text{CdTe}$ photoanode are found to be 5.97 mA cm^{-2} (Supplementary Fig. 15) and 11.84 mA cm^{-2} (Supplementary Fig. 28), respectively. These values are in close agreement with the photocurrent densities obtained from the LSV measurements. The consistency between the two sets of photocurrent density demonstrates the accuracy of our AM 1.5 G simulator in simulating sunlight, ensuring the reliability and accuracy of J–V and IPCE measurements. The PEC performance of this $\text{Ag}/\text{Ag}:\text{In}_2\text{S}_3/\text{In}_2\text{S}_3/\text{CdTe}/\text{NiO}_x/\text{TiO}_2/\text{Ni}$ photoanode stands out among many In_2S_3 -based photoanodes reported to date (Supplementary Table 8). The ABPE of the $\text{Ag}/\text{Ag}:\text{In}_2\text{S}_3/\text{In}_2\text{S}_3/\text{CdTe}/\text{NiO}_x/\text{TiO}_2/\text{Ni}$ photoanode reaches 3.03% (Fig. 1c), surpassing the 1.85% efficiency of the photoanode without CdTe (Supplementary Fig. 14b). The improved PEC performance can be attributed to the formation of a bandgap-matched $\text{In}_2\text{S}_3/\text{CdTe}$ p–n junction. The built-in

electric field at the junction enhances the driving force for carrier separation, facilitating the migration of photogenerated electrons and holes in opposite directions. As a result, the efficient separation of electron–hole pairs is promoted, and carrier recombination is suppressed.

Stability remains a critical issue for practical solar water splitting application. Metal sulfides, including In_2S_3 , often suffer from corrosion in alkaline solutions. The highest reported stability for In_2S_3 photoanode was about 20 h³⁷. In contrast, the photocurrent of the $\text{Ag}/\text{Ag}:\text{In}_2\text{S}_3/\text{In}_2\text{S}_3/\text{CdTe}/\text{NiO}_x/\text{TiO}_2/\text{Ni}$ photoelectrode remained stable over 60 h at 1.23 V *vs.* RHE under AM 1.5 G illumination in 1 M NaOH (Fig. 1d). During a 10 h long test, the Faradaic efficiency for oxygen remained close to 100%, with no significant decrease, indicating that the anodic photocurrent originated from oxygen evolution rather than electrode degradation or other competitive oxidation processes (Supplementary Fig. 16). Without the 10 nm ALD-deposited TiO_2 protective layer, the $\text{Ag}/\text{Ag}:\text{In}_2\text{S}_3/\text{In}_2\text{S}_3/\text{CdTe}/\text{NiO}_x/\text{Ni}$ photoelectrode remains stable for approximately 4 h, after which the photocurrent density declines rapidly with further extension of the duration (Supplementary Fig. 17). This demonstrates that the TiO_2 protective layer can effectively protect the photoanode from damage in alkaline solution, further improving the stability of the device.

Construction of semi-transparent $\text{Ag}/\text{In}_2\text{S}_3$ ohmic contact

To elucidate the impact of Ag incorporation on carrier transport in In_2S_3 photoanodes, comparative performance analyses were conducted on In_2S_3 devices with and without Ag layers. The FTO/ In_2S_3 photoanode exhibits a photocurrent density of 2.0 mA cm^{-2} at 1.23 V *vs.* RHE. However, the FTO/ $\text{Ag}:\text{In}_2\text{S}_3/\text{In}_2\text{S}_3$ photoanode exhibited a current density of 3.8 mA cm^{-2} at 1.23 V *vs.* RHE (Fig. 2a). This indicates that the ohmic contact reduces the potential drop under reverse bias across the FTO/ In_2S_3 interface, while Ag gradient doping enhances the intrinsic conductivity of In_2S_3 , thereby facilitating more efficient electron collection from In_2S_3 to FTO. Electrochemical impedance spectroscopy (EIS) measurements were further conducted to compare the charge-transfer resistance of In_2S_3 and $\text{Ag}/\text{Ag}:\text{In}_2\text{S}_3/\text{In}_2\text{S}_3$ photoanodes. The inset of Fig. 2b presents the equivalent circuit employed for fitting the impedance data. In comparison to the In_2S_3 photoanode, a smaller arc radius was observed for the $\text{Ag}/\text{Ag}:\text{In}_2\text{S}_3/\text{In}_2\text{S}_3$ photoanode (Fig. 2b). The J–V curve of the FTO/ $\text{In}_2\text{S}_3/\text{Au}$ device displays nonlinear bending, indicating significant contact resistance and the inability to establish an ideal ohmic contact. In contrast, the FTO/ $\text{Ag}:\text{In}_2\text{S}_3/\text{Ag}/\text{In}_2\text{S}_3/\text{Au}$ devices exhibit good linear output characteristics at room temperature (Fig. 2c). These phenomena are due to the synergistic effect of the ohmic contact provided by metallic Ag as well as the gradient doping of Ag in In_2S_3 , which enhances the conductivity of the In_2S_3 layer and optimizes the interfacial contact properties, thereby improving charge carrier transport efficiency.

To further elucidate the effect of Ag on the morphology and transparency of In_2S_3 photoanodes, film characterization was conducted on In_2S_3 devices with and without Ag layers. In_2S_3 films were annealed in air at 300 °C for 10 min to promote crystallization. The surface of FTO/ In_2S_3 thin film remains flat with uniform grain size after annealing (Supplementary Fig. 18a), whereas the FTO/ $\text{Ag}/\text{In}_2\text{S}_3$ thin film transforms into a granular structure after annealing (Supplementary Fig. 18b). Sputtering a 10 nm Ag film onto FTO glass reduces its transmittance from ~85 to 42%, indicating a substantial decline in optical transparency. This pronounced reduction in transmittance severely impacts the performance of back-illuminated photoanode devices. After annealing the FTO/Ag film at 300 °C for 10 min, the transmittance of the device increased to ~70% (Fig. 2d). In order to analyze the reason for the increase in transmittance of Ag film after annealing, the morphology of FTO/Ag devices before and after annealing was characterized. In the unannealed state, Ag film presents a uniformly covered small particle structure. However, the Ag film

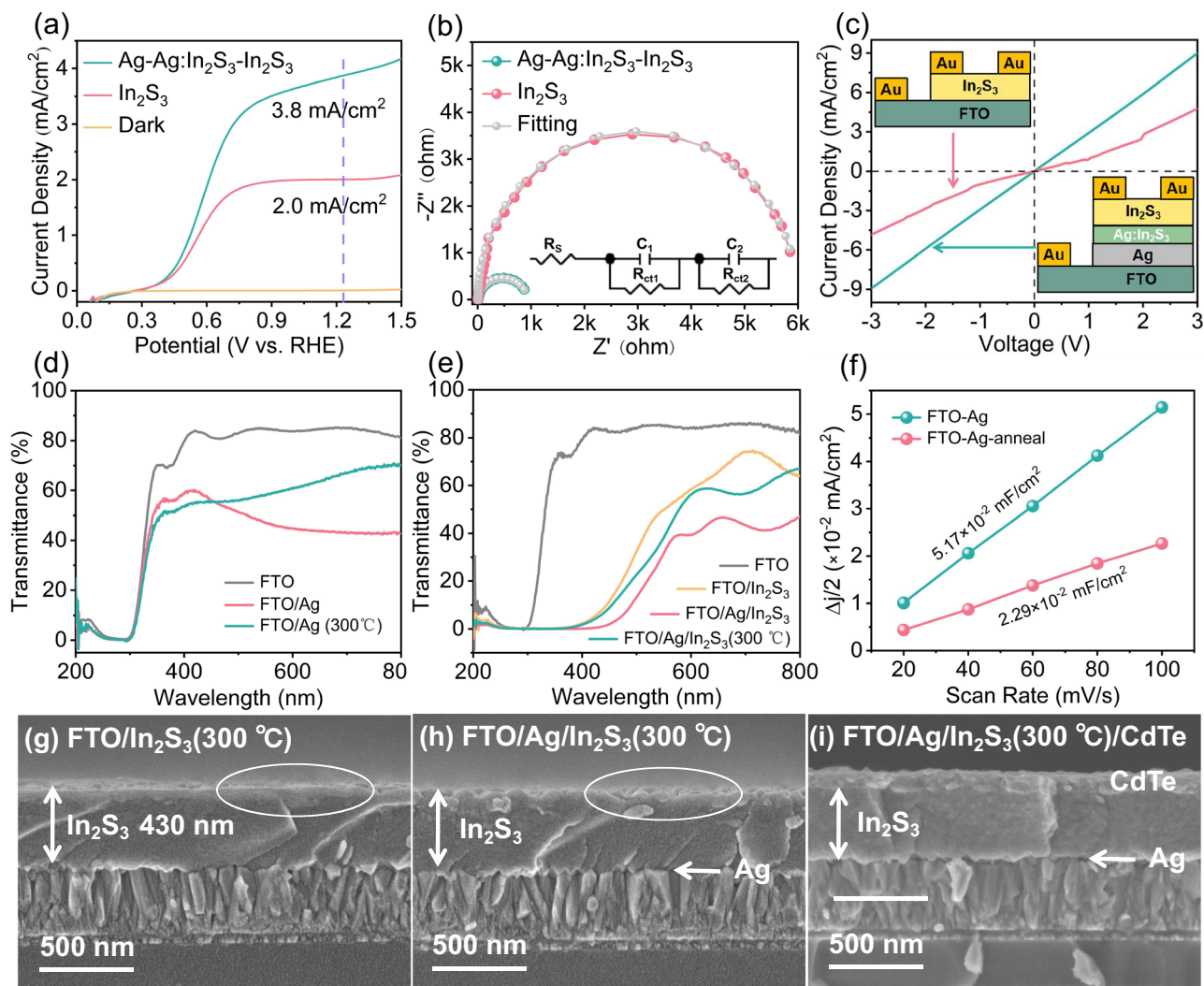


Fig. 2 | Ohmic contact and surface morphology changes of Ag/In₂S₃. **a** J–V curves of FTO/Ag/Ag:In₂S₃/In₂S₃ and FTO/In₂S₃ devices. **b** Nyquist plots of Ag/Ag:In₂S₃/In₂S₃ and In₂S₃ devices (inset: the equivalent circuit). **c** Analysis of ohmic contacts in FTO/In₂S₃/Au and FTO/Ag/Ag:In₂S₃/Au devices. **d** Comparing the transmission spectra of unannealed FTO/Ag and annealed FTO/Ag (300 °C). **e** Comparing the transmission spectra of unannealed FTO/Ag/In₂S₃ and annealed

FTO/Ag/In₂S₃ (300 °C). **f** Corresponding charging current density difference as a function of scan rates for FTO/Ag and FTO/Ag (anneal). The cross-sectional SEM images of **g** FTO/In₂S₃ (300 °C), **h** FTO/Ag/In₂S₃ (300 °C), **i** FTO/Ag/In₂S₃ (300 °C)/CdTe (300 °C). The experiments are conducted without iR compensation. Source data are provided in the Source Data file.

annealed at 300 °C showed aggregation of Ag particles and an increase in particle size, thereby improving the transmittance (Supplementary Fig. 19). The corresponding electrochemical active surface area (ECSA) test (Supplementary Fig. 20) shows that the specific surface area of annealed Ag was reduced compared to that of unannealed Ag (Fig. 2f). This further proves that Ag particles tend to aggregate during the annealing process. Simultaneously, it was observed that the transmittance of the annealed FTO/Ag/In₂S₃ device (where the Ag and In₂S₃ thin films were annealed together) was enhanced compared to the unannealed FTO/Ag/In₂S₃ device (Fig. 2e). Cross-sectional scanning electron microscope (SEM) shows that the Ag layer cannot be observed due to its thin thickness of only 10 nm. The top of the FTO/In₂S₃ (300 °C) section was flat (Fig. 2g), while the FTO/Ag/In₂S₃ (300 °C) section showed a concave-convex structure (Fig. 2h). This structure is consistent with the surface morphology changes observed in the top-view SEM images. In the end, an FTO/Ag/In₂S₃ structure was obtained that preserves the transparency of the device while enhancing the charge-transfer dynamics of the In₂S₃ photoanode.

To verify the stability of annealed thin films, further analysis was conducted on the elemental composition and distribution of In₂S₃ and

CdTe thin films after annealing. The elemental ratios were determined to be ~2:3 for In to S in the In₂S₃ film (Supplementary Table 4) and 1:1 for Cd to Te in the CdTe film (Supplementary Table 5) according to energy dispersive spectroscopy (EDS). In addition, top-view EDS elemental mappings indicated that all elements were homogeneously distributed in the lateral plane (Supplementary Figs. 21 and 22). The cross-sectional top-view EDS analysis of the FTO/In₂S₃ thin films indicates that the bottom layer primarily consisted of the elemental constituents of glass, namely Si and O (Supplementary Fig. 23e, f). The middle layer contained predominantly Sn and O from the FTO (Supplementary Fig. 23d, e), while the top layer exhibited overlapping of In and S elements (Supplementary Fig. 23b, c). Notably, clear boundaries could be observed between the layers, with no vertical diffusion detected (Supplementary Fig. 23). This suggests that the elemental composition within each layer remained stable throughout the annealing process.

Formation of p–n junction for enhanced charge separation

To investigate the impact of the p–n junction on photogenerated charge separation and transport, the band structure of In₂S₃ and CdTe heterojunction photoelectrodes was analyzed. The absorption edge of

the In_2S_3 film is observed within the range of 500–600 nm, whereas the absorption edge of CdTe film extends to longer wavelengths (Fig. 3a). The bandgap of In_2S_3 and CdTe are determined to be 2.08 eV and 1.53 eV, respectively, based on the intercepts in the Tauc plots (Fig. 3b). Ultraviolet photoelectron spectroscopy (UPS) revealed that the valence band maximum (VBM) of the In_2S_3 film (−6.35 eV) is 0.72 eV lower than the highest occupied molecular orbit (HOMO) of the CdTe film (−5.63 eV) (Fig. 3d and Supplementary Fig. 24). However, the energy difference between the VBM of the CdTe film and the HOMO (−5.49 eV) of the HTL is only 0.14 eV, which helps reduce the energy loss and facilitates charge transfer (Supplementary Fig. 25)⁵². This energy level alignment, which is advantageous for extracting photo-generated holes from In_2S_3 to NiO_x , results from the increased built-in potential for enhanced charge separation. The bandgap of Si is 1.12 eV, allowing it to absorb light in the wavelength range of 200–1100 nm. Therefore, we performed light absorption tests on In_2S_3 and CdTe thin films across a broader wavelength range (Supplementary Fig. 26). The results show that In_2S_3 hardly absorbs light beyond 600 nm, while CdTe exhibits negligible absorption above 900 nm. Furthermore, due to the thin CdTe film, light in the 600–1100 nm wavelength range can pass through the photoanode and reach the Si photocathode, thereby enabling unbiased photoelectrochemical water splitting.

The impact of the p–n junction on charge separation was further elucidated by analyzing the changes in the Fermi level of the $\text{In}_2\text{S}_3/\text{CdTe}$ heterojunction before and after illumination. Firstly, the conductivity type and carrier concentration of In_2S_3 and $\text{In}_2\text{S}_3/\text{CdTe}$ are investigated using Mott-Schottky (M–S) curves (Fig. 3c). It can be inferred that In_2S_3 is an n-type semiconductor based on its positive slope. The M–S plot of $\text{In}_2\text{S}_3/\text{CdTe}$ exhibits an inverted “V” shape, indicating the coexistence of n-type and p-type conductivity in the $\text{In}_2\text{S}_3/\text{CdTe}$ samples. Meanwhile, the M–S plot of the $\text{In}_2\text{S}_3/\text{CdTe}$ heterojunction shows that the slope of the positive-slope region is smaller than that of the M–S plot slope of the In_2S_3 sample, indicating that the carrier density of the $\text{In}_2\text{S}_3/\text{CdTe}$ heterojunction is higher. The negative slope in the latter half of the curve confirms that CdTe is a p-type semiconductor. Before contact, In_2S_3 behaves as an n-type semiconductor, with its Fermi level positioned near the conduction band minimum, whereas CdTe, as a typical p-type semiconductor, possesses a Fermi level situated close to the valence band maximum. After the formation of p–n heterojunction, the Fermi levels of the two semiconductors align (Fig. 3e). Under illumination, electrons from CdTe are rapidly injected into the conduction band of In_2S_3 , while holes from In_2S_3 are promptly captured by the valence band of CdTe (Fig. 3f). Crucially, this charge separation and transport are enhanced at the $\text{In}_2\text{S}_3/\text{CdTe}$ interface by the built-in electric field, which directs from n- In_2S_3 to p-CdTe. The holes collected in CdTe can be further utilized by NiO_x and a cocatalyst for water oxidation, effectively overcoming electron–hole recombination and enhancing charge separation efficiency, leading to improved PEC performance.

To verify the effect of band alignment on the carrier lifetime of devices, we fabricated In_2S_3 and $\text{In}_2\text{S}_3/\text{CdTe}$ p–n heterojunctions^{37,39,71}. The steady-state photoluminescence (PL) quenching for the $\text{In}_2\text{S}_3/\text{CdTe}$ heterojunction sample is markedly pronounced, suggesting a more efficient hole extraction process between the In_2S_3 and CdTe (Fig. 4a). The carrier lifetimes for In_2S_3 , CdTe and $\text{In}_2\text{S}_3/\text{CdTe}$ heterojunction sample were quantified using time-resolved photoluminescence (TRPL) tests (Fig. 4b)^{72,73}. The findings reveal that the carrier lifetime of the $\text{In}_2\text{S}_3/\text{CdTe}$ heterojunction (28.26 ns) is extended compared to In_2S_3 (6.83 ns) and CdTe (11.92 ns) (Supplementary Table 6). This enhancement suggests that the heterojunction enhances carrier transport and reduces carrier recombination, thereby extending the carrier lifetime.

Unlike the LSV test in PEC, the photocurrent density–voltage (J–V) characteristics of solid-state devices are measured by the charge transport mechanisms (such as electron or hole conduction) within the

solid-state device, rather than through the conduction of the electrolyte solution. This characteristic provides a more direct reflection of the open-circuit voltage that the photoanode material we prepared can deliver under illumination, and is mutually validated with the onset potential observed in LSV measurements. The open-circuit voltage (V_{oc}) of In_2S_3 and $\text{In}_2\text{S}_3/\text{CdTe}$ p–n heterojunctions was compared to verify the role of the p–n junction in the photoanode. The 80 nm Au electrode was evaporated on top of the TiO_2 layer, obtained solid-state devices with the structures $\text{FTO}/\text{Ag}/\text{Ag}:\text{In}_2\text{S}_3/\text{In}_2\text{S}_3/\text{CdTe}/\text{NiO}_x/\text{TiO}_2/\text{Au}$ and $\text{FTO}/\text{Ag}/\text{Ag}:\text{In}_2\text{S}_3/\text{In}_2\text{S}_3/\text{NiO}_x/\text{TiO}_2/\text{Au}$ (Supplementary Fig. 27). The J–V characteristics of the above solid-state devices were evaluated under simulated AM 1.5 G illumination (Fig. 4c). The $\text{In}_2\text{S}_3/\text{CdTe}$ heterojunction device exhibits superior performance, achieving a V_{oc} of 0.71 V and a short-circuit current (J_{sc}) of 11.90 mA/cm^2 . In contrast, the In_2S_3 device without p–n heterojunction shows a V_{oc} of 0.60 V and a J_{sc} of 6.12 mA/cm^2 (Supplementary Table 7). Moreover, $\text{Ag}/\text{Ag}:\text{In}_2\text{S}_3/\text{In}_2\text{S}_3/\text{CdTe}/\text{NiO}_x/\text{TiO}_2/\text{Ni}$ photoanodes achieves a higher photocurrent density of 12.20 mA/cm^2 at 1.23 V *vs.* RHE compared to $\text{Ag}/\text{Ag}:\text{In}_2\text{S}_3/\text{In}_2\text{S}_3/\text{NiO}_x/\text{TiO}_2/\text{Ni}$ photoanodes (6.1 mA/cm^2), and a lower onset potential of 0.35 V *vs.* RHE compared to 0.46 V for the latter configuration (Fig. 4d). The integrated current density of the $\text{In}_2\text{S}_3/\text{CdTe}$ Photoanode is 11.84 mA/cm^2 (Supplementary Fig. 28), which is in close agreement with the photocurrent density obtained from the LSV test. Due to the narrow bandgap of CdTe, which has an absorption edge around 800 nm, the incorporation of CdTe into the photoanode device extends the overall absorption range of the device to ~800 nm, thereby enhancing its light absorption (Supplementary Fig. 29). The enhanced PEC performance of the $\text{In}_2\text{S}_3/\text{CdTe}$ p–n heterojunction is attributed to its ability to facilitate efficient carrier transport by forming a built-in electric field that promotes carrier separation. In addition, CdTe makes a significant contribution to light absorption within a certain absorption range.

Construction of a standalone unbiased PEC tandem cell

To fabricate the PEC tandem cell for unassisted overall solar water splitting, we prepared a back-illuminated Si (B-Si) photocathode (Supplementary Fig. 30). A 10 nm dense TiO_2 protective layer was deposited on the reaction side of the B-Si photocathode⁷⁴. A layer of soda-lime glass (SLG) was applied to the illuminated side of the B-Si photocathode, functioning as a transparent protective layer and ensuring effective light absorption owing to its high transmittance. An Ag layer (200 nm) was deposited onto the edge region of the light-absorbing surface of the B-Si photocathode to serve as a back contact. A 3-nm-thick Pt layer was deposited as a catalyst on the surface of the TiO_2 protective layer. Finally, the Si photocathode was encapsulated using an epoxy resin adhesive and silver paste. During the test, the entire SLG (yellow area) is exposed to sunlight, while the region within the white box designates the working area of the photocathode (Supplementary Fig. 31b). Image J software was employed to precisely measure the effective working area of the device, which was determined to be 0.612 cm^2 (Supplementary Fig. 31a). The fabricated B-Si photocathode was tested in a 1 M NaOH solution, achieving a photocurrent density of 29.73 mA/cm^2 . A light blocking test was conducted by placing the $\text{Ag}/\text{Ag}:\text{In}_2\text{S}_3/\text{In}_2\text{S}_3/\text{CdTe}/\text{NiO}_x/\text{TiO}_2/\text{Ni}$ photoanode in front of the B-Si photocathode, resulting in a photocurrent density of 13.03 mA/cm^2 . This clarifies the effectiveness of the semi-transparent feature of photoanodes and the pristine PEC performance of the B-Si photocathode. The performance decrease is attributed to partial absorption of sunlight as it passes through the front semi-transparent photoanode before reaching the B-Si photocathode (Supplementary Fig. 32).

To illustrate the practical application potential of the semi-transparent photoanode, unassisted overall solar water splitting was demonstrated using a PEC tandem cell composed of the $\text{Ag}/\text{Ag}:\text{In}_2\text{S}_3/\text{In}_2\text{S}_3/\text{CdTe}/\text{NiO}_x/\text{TiO}_2/\text{Ni}$ photoanode and B–Si photocathode. UV–vis

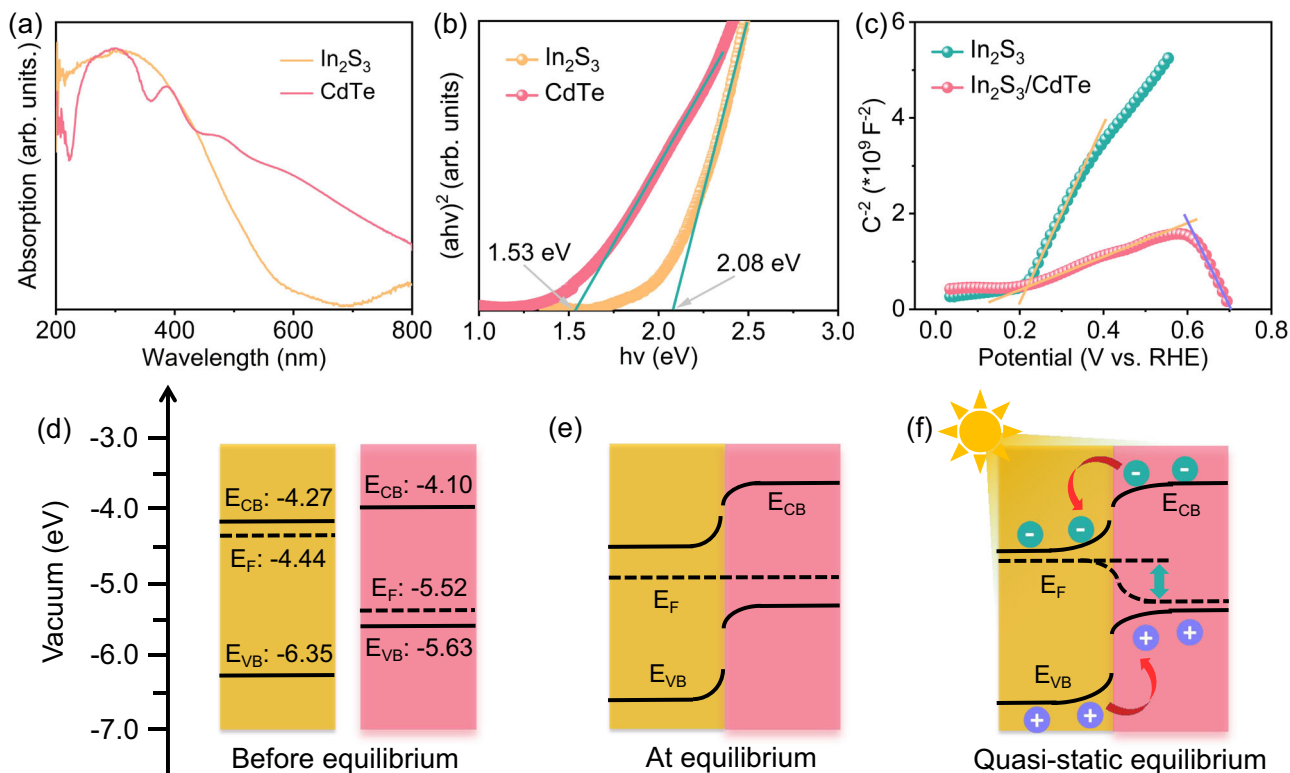


Fig. 3 | Band alignments for In_2S_3 and CdTe. **a** UV-vis absorption spectra of the In_2S_3 and CdTe films. **b** Tauc plots of the In_2S_3 films and the CdTe films. **c** The M-S analysis curve of In_2S_3 and $\text{In}_2\text{S}_3/\text{CdTe}$. Schematic energy level alignment **d** before

equilibrium, **e** at equilibrium, and **f** quasi-static equilibrium of the In_2S_3 and CdTe films. Source data are provided in the Source Data file.

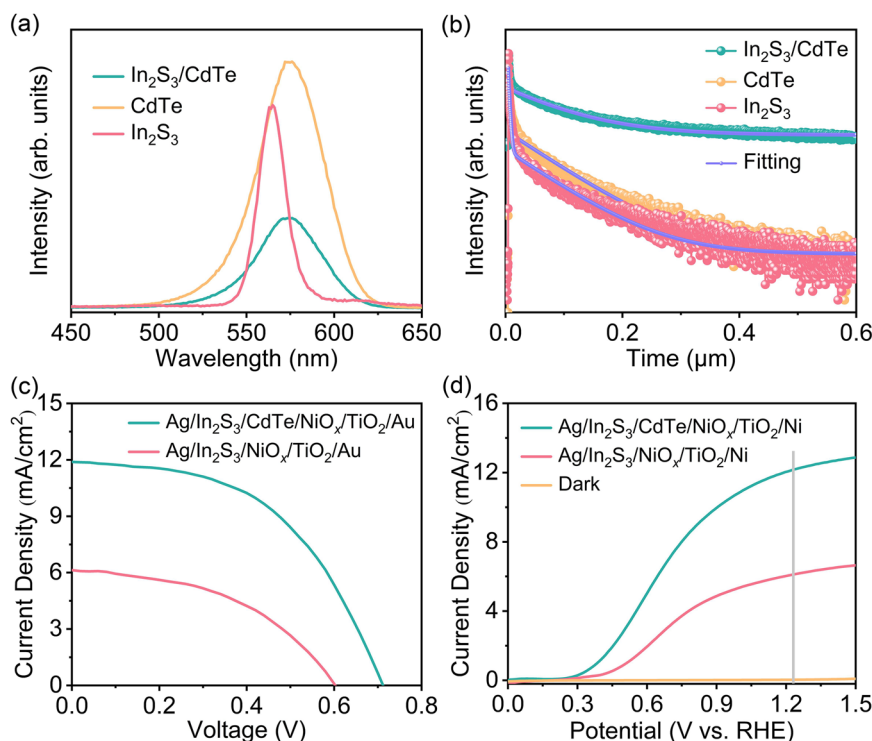


Fig. 4 | The impact of band alignment on the carrier lifetime in In_2S_3 and $\text{In}_2\text{S}_3/\text{CdTe}$ heterojunction devices. **a** PL spectra of In_2S_3 , CdTe and $\text{In}_2\text{S}_3/\text{CdTe}$ heterojunction. **b** PL decay curves of In_2S_3 , CdTe and $\text{In}_2\text{S}_3/\text{CdTe}$ heterojunction. **c** Solid-state J-V curves of FTO/Ag/Ag/ $\text{In}_2\text{S}_3/\text{In}_2\text{S}_3/\text{CdTe}/\text{NiO}_x/\text{TiO}_2/\text{Au}$ and FTO/Ag/Ag/

$\text{In}_2\text{S}_3/\text{In}_2\text{S}_3/\text{NiO}_x/\text{TiO}_2/\text{Au}$ devices. **d** PEC J-V curves of FTO/Ag/Ag/ $\text{In}_2\text{S}_3/\text{In}_2\text{S}_3/\text{CdTe}/\text{NiO}_x/\text{TiO}_2/\text{Ni}$ and FTO/Ag/Ag/ $\text{In}_2\text{S}_3/\text{In}_2\text{S}_3/\text{NiO}_x/\text{TiO}_2/\text{Ni}$ devices. The experiments are conducted without iR compensation. Source data are provided in the Source Data file.

spectroscopy confirms the high transparency of the $\text{In}_2\text{S}_3/\text{CdTe}$ photoanode (Supplementary Fig. 33), enabling light to transmit through the front semi-transparent photoanode and reach the B-Si photocathode during testing (Fig. 5b). In the three-electrode configuration, the J-V curves of the $\text{In}_2\text{S}_3/\text{CdTe}$ photoanode and B-Si photocathode (behind $\text{In}_2\text{S}_3/\text{CdTe}$ photoanode) can be obtained, respectively, where the intersection of the two J-V curves suggests a theoretical photocurrent of 4.15 mA/cm^2 (Fig. 5a). An actual photocurrent of 4.09 mA/cm^2 was achieved using an unbiased two-electrode configuration, which is slightly lower than the anticipated 4.15 mA/cm^2 . In addition, the PEC cell demonstrated stable performance under continuous illumination for 20 h (Fig. 5b).

In addition, the theoretical STH efficiency of the PEC cell composed of a semi-transparent photoanode and B-Si photocathode is 5.1% (Fig. 5a). The Faradaic efficiency for hydrogen was quantified using gas chromatography, further revealing that the actual STH efficiency is 5.03% (Supplementary Fig. 34), which is in close agreement with the theoretical value, demonstrating significant potential for practical applications. Comparative analysis (Supplementary Fig. 35a) shows that the photocurrent density and stability of the In_2S_3 -based photoanode developed in this study are superior to those reported in previous studies (Supplementary Table 8). The STH efficiency was calculated to be 5.1% from the unassisted two-electrode configuration, marking an impressive efficiency reported for such unbiased PEC water splitting devices combining Si-based photocathodes with an exclusively inorganic photoanode (Supplementary Fig. 35b and Supplementary Table 9). Moreover, the STH efficiency of the $\text{Ag}/\text{Ag}:\text{In}_2\text{S}_3/\text{In}_2\text{S}_3/\text{CdTe}/\text{NiO}_x/\text{TiO}_2/\text{Ni}$ photoanode and Si photocathode tandem cell remains relatively high compared to many other multilayer photoelectrodes with charge transport layers (Supplementary Table 10). Therefore, our study provides a low-cost and high-efficiency strategy for constructing p-n heterojunction photoelectrodes to enhance the performance of PEC devices. It also provides critical insights for the future advancement and design of unbiased PEC water splitting systems.

Discussion

This work describes the design and fabrication of a semi-transparent photoanode with Ag and CdTe on the illuminated and back side of the In_2S_3 layer, enhancing carrier separation and transport, thereby enabling unbiased solar water splitting. Specifically, the introduction of an annealed Ag layer at the FTO/ In_2S_3 interface forms a semi-transparent ohmic contact and induces Ag gradient doping, effectively resolving the conflict between the light-shielding effect of the metal

and the barrier to majority carrier transport across the interface. Furthermore, the thin CdTe layer and In_2S_3 form p-n heterojunctions with properly aligned energy levels, generating effective built-in electric fields while avoiding the light-shielding issues associated with thick CdTe films. As a result, the semi-transparent $\text{In}_2\text{S}_3/\text{CdTe}$ photoanode achieves a notable photocurrent density of 12.2 mA/cm^2 at 1.23 V vs. RHE . In addition, the semi-transparent properties of the $\text{Ag}/\text{Ag}:\text{In}_2\text{S}_3/\text{In}_2\text{S}_3/\text{CdTe}/\text{NiO}_x/\text{TiO}_2/\text{Ni}$ photoanode make it well-suited for pairing with the back-illuminated Si photocathode, resulting in a 5.10% STH efficiency in an independent unbiased PEC tandem cell. This work clearly demonstrates the suitability of the n- In_2S_3 bandgap and its potential for forming heterojunctions with p-type semiconductors, offering valuable insights for future multi-component tandem photoelectrodes.

Methods

Materials

Sodium hydroxide (NaOH , $\geq 99\%$) was purchased from Shanghai Aladdin Industrial Corporation. Titanium (IV) i-propoxide (TTIP, 99.999%) was purchased from Suzhou Fornano Electronics Technology Co. Ltd. The Ni and Ag sputtering targets both had a thickness of 3 mm and a purity of 99.99%. The Pt sputtering target has a thickness of 2 mm and a purity of 99.99%. The In_2S_3 and CdTe targets are 4 mm thick, each with a 2 mm copper backing, and both have a purity of 99.99%. All the sputtering targets had a diameter of 50.8 mm and were purchased from ZhongNuo Advanced Materials (Beijing) Technology Co., Ltd. High-purity water ($18.25 \text{ M}\Omega \text{ cm}$) supplied by an ultrapure water Purification System was used in the entire experimental process. All reagents were used directly without further purification.

Fabrication of the photoanode

Ultrasonic cleaning of FTO glass substrates was first performed in a diluted glass cleaning solution for 30 min, followed by treatment in ultrapure water for an additional 20 min. Subsequently, the FTO glass was dried under a nitrogen stream and subjected to ultraviolet ozone treatment for 10 min. A 10 nm thick Ag film was deposited by DC magnetron sputtering. Prior to deposition, the chamber was evacuated to a base pressure of 10^{-5} Pa . High-purity argon gas was then introduced at a flow rate of 20 sccm, establishing a working pressure of 1.0 Pa. The sputtering process was conducted at a power of 10 W. In_2S_3 film was deposited by RF sputtering, the working pressure was held at 1.0 Pa, and the sputtering power was kept at 60 W. The film was annealed at 300°C for 10 min to improve crystallinity. Finally, the In_2S_3 film with a thickness of approximately 450 nm was obtained. After

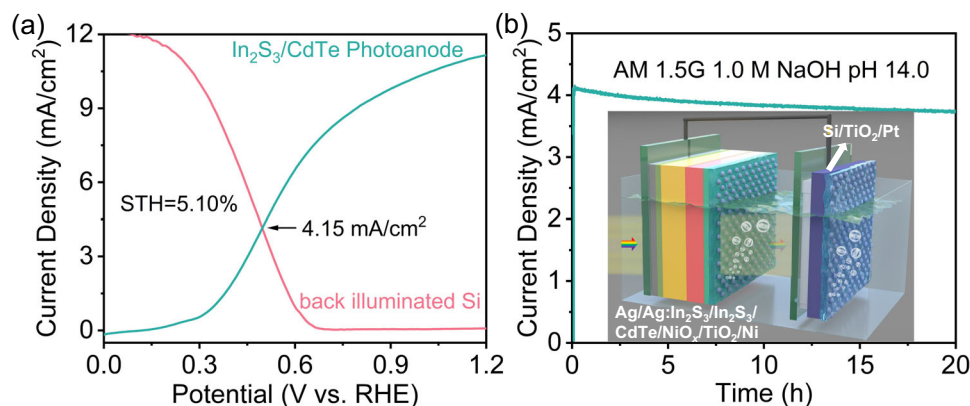


Fig. 5 | Unbiased water splitting performance of tandem device under simulated AM 1.5G illumination. **a** J-V curves of illuminated Si photocathode (behind $\text{In}_2\text{S}_3/\text{CdTe}$ photoanode) and $\text{In}_2\text{S}_3/\text{CdTe}$ photoanode for three-electrode configuration, respectively, **b** the current-time curves for two-electrode cell with stirring.

Inset: schematic illustration of the unbiased PEC overall water splitting tandem device. The experiments are conducted without iR compensation. Source data are provided in the Source Data file.

cooling to room temperature, CdTe film was deposited by RF sputtering, the working pressure was held at 1.0 Pa, and the sputtering power was kept at 50 W. The CdTe film was subsequently annealed at 300 °C for 10 min to achieve a thickness of approximately 80 nm. The NiO_x film was deposited by RF sputtering, with the Ar gas flow set at 20 sccm and the O₂ gas flow set at 10 sccm. After sputtering, the NiO_x film was annealed at 300 °C for 10 min at room temperature to form a 25 nm NiO_x film, which served as the hole transport layer. A TiO₂ protective layer was deposited via ALD at a substrate temperature of 150 °C. TTIP (70 °C) was employed as the titanium precursor, with deionized water (25 °C) serving as the oxygen source. Each ALD cycle consisted of a 0.3 s TTIP pulse, an 8 s N₂ purge, a 0.1 s H₂O pulse, and a subsequent 8 s N₂ purge. Ni was deposited using DC magnetron sputtering. The deposition process was carried out at 1 Pa and 10 W for 20 s, resulting in a Ni catalyst layer with a thickness of 3 nm.

Fabrication of the solid-state device

Ag, In₂S₃, CdTe, and NiO_x films were sequentially deposited on FTO/glass substrates using magnetron sputtering. Then, a 10 nm TiO₂ layer was deposited on the NiO_x film by ALD. The fabrication methods for these films are identical to those described in the “Fabrication of the photoanode” section. Subsequently, an 80 nm Au layer was evaporated on the TiO₂ surface to serve as the top electrode of the solid-state device. The effective area of each device is 0.09 mm².

Fabrication of the photocathode

Czochralski (CZ) grown n-type crystalline silicon (c-Si) wafers were selected as the substrate material due to their high quality and uniformity. The c-Si wafer surfaces were initially textured using an alkaline solution composed of potassium hydroxide (KOH) and isopropyl alcohol (IPA). After surface texturing, the wafers underwent a standard RCA cleaning sequence, followed by immersion in a 5% hydrofluoric acid (HF) solution (60 s) to remove the native silicon oxide layer. Following surface pre-treatment, the Si wafer was placed in a plasma-enhanced chemical vapor deposition (PECVD) system, where intrinsic amorphous silicon (a-Si) thin films with a thickness of approximately 5 nm were deposited on both sides to achieve interface passivation. In the next step, n⁺- and p⁺-a-Si layers were deposited on the intrinsic a-Si films to form selective carrier transport contact structures, which are essential for reducing recombination losses and improving device performance. To protect the Si photoelectrode, a 10 nm amorphous TiO₂ layer was deposited at 150 °C. DC magnetron sputtering was employed to deposit a Pt catalytic layer. A constant pressure of 1 Pa and a power of 10 W were maintained, and the deposition time was optimized to achieve a 3 nm film thickness.

PEC measurements

Preparation method of NaOH electrolyte: A total of 8.0 g of NaOH was accurately weighed and gradually added to 200 mL of deionized water in a plastic container. The mixture was continuously stirred using a magnetic stirrer until the NaOH was completely dissolved, resulting in a homogeneous alkaline solution with a final concentration of 1.0 mol/L. The pH of the prepared solution, as measured using a pH meter, was 14.0 ± 0.2. To ensure its chemical stability and effectiveness, the solution was used on the same day of preparation.

Before electrochemical testing, the Hg/HgO reference electrode was calibrated using a 1.0 M NaOH solution to ensure the accuracy and repeatability of its potential. Before the experiment, high-purity hydrogen gas was introduced into the solution and allowed to saturate for 30 min to establish a stable electrochemical environment. Pt foil was employed as both the working and counter electrodes, while a Hg/HgO electrode was used as the reference electrode.

PEC measurements were carried out using a standard three-electrode configuration. The In₂S₃ photoanode was used as the working electrode, a saturated Hg/HgO electrode served as the

reference electrode, and platinum foil functioned as the counter electrode to complete the electrochemical circuit. The voltage values obtained during the experiment were converted to potentials relative to the reversible hydrogen electrode using the following equation:

$$E_{\text{RHE}} = E_{\text{Hg/HgO}} + 0.059\text{pH} + 0.098 \quad (1)$$

During the testing process, a solar simulator (AM 1.5 G, SAN-EI ELECTRIC XES-40S3-TT) provided a stable and continuous light source, while experimental data were collected using an electrochemical workstation (IVIUM Technologies, Vertex.1 A.EIS).

The ABPE was determined under illumination according to the following equation:

$$\text{ABPE} = J \times \frac{1.23 - |V_b|}{P} \times 100\% \quad (2)$$

where J represents the photocurrent density under illumination, V_b is the applied potential versus the reversible hydrogen electrode, and P denotes the intensity of the incident light.

The STH efficiency was calculated according to the following equation:

$$\text{STH}(\%) = \frac{J_{\text{OP}} \times 1.23}{P} \times \text{FE}_{\text{H}_2} \quad (3)$$

where J_{OP} represents the operating photocurrent density produced by the integrated tandem device, and P denotes the intensity of the incident solar illumination. The theoretical value of STH is calculated using FE_{H_2} equal to 100%. H₂ and O₂ were quantified using an on-line gas chromatography system (Agilent Technologies, Inc., GC7890B).

The IPCE was measured under monochromatic illumination and calculated using the following equation:

$$\text{IPCE} = \frac{\left[\frac{1240}{\lambda} \times (I_{\text{light}} - I_{\text{dark}}) \right]}{P} \times 100\% \quad (4)$$

where λ is wavelength, P represents the power density of the incident light at the specified wavelength, I_{light} and I_{dark} represent the current densities measured under illumination and in the dark, respectively.

The ECSA was evaluated by determining the double-layer capacitance (C_{dl}) in 1.0 M NaOH solution and calculated using the following equation:

$$\text{ECSA} = \frac{C_{\text{dl}}}{C_s} \quad (5)$$

In alkaline media, the specific double-layer capacitance C_s is conventionally considered to be 0.040 mF cm⁻².

Material characterization

The microstructure and surface morphology of the photoelectrode samples were characterized using field emission scanning electron microscopy (FESEM, Hitachi Regulus 8100). To investigate the photoluminescence properties of the material, its PL spectrum was measured at an excitation wavelength of 510 nm using a steady-state spectroscopy system (Edinburgh Instruments Ltd. FLS980). In addition, the TRPL measurements were conducted with a time-resolved spectrometer (PicoQuant FluoQuant 300) to analyze the carrier lifetime. The thicknesses of the Ag, Ni, Pt, and TiO₂ thin films were determined through optical characterization using the M-2000D spectroscopic ellipsometer manufactured by J.A. Woollam Co., Ltd. The transmission spectrum of the photoelectric device was measured at room temperature using the UV-2550 spectrophotometer manufactured by Shimadzu Corporation. XPS measurements were

conducted on a K-Alpha⁺ spectrometer system manufactured by Thermo Scientific, which is equipped with a monochromatic Al K α X-ray source.

Data availability

All data generated or analyzed during this study are included in the published article and its Supplementary Information. Source data are provided with this paper.

References

- Yao, T. T., An, X. R., Han, H. X., Chen, J. Q. & Li, C. Photoelectrocatalytic materials for solar water splitting. *Adv. Energy Mater.* **8**, 1800210 (2018).
- Chang, X. X., Wang, T., Yang, P. P., Zhang, G. & Gong, J. L. The development of cocatalysts for photoelectrochemical CO₂ reduction. *Adv. Mater.* **31**, 1804710 (2019).
- Feng, C. & Li, Y. B. Self-healing mechanisms toward stable photoelectrochemical water splitting. *Chin. J. Catal.* **60**, 158–170 (2024).
- Zhang, S. Y., Du, P. Y. & Lu, X. Q. Advancements in semiconductor-based interface engineering strategies and characterization techniques for carrier dynamics in photoelectrochemical water splitting. *Sci. China Mater.* **67**, 1379–1392 (2024).
- Huan, Z. L., Fu, H. P., Zheng, X. R. & Ji, H. M. Disordered rocksalts with lattice oxygen activation as efficient oxygen evolution electrocatalysts. *Trans. Tianjin Univ.* **29**, 304–312 (2023).
- Mesa, C. A. et al. Multihole water oxidation catalysis on hematite photoanodes revealed by operando spectroelectrochemistry and DFT. *Nat. Chem.* **12**, 82–89 (2020).
- Lee, D. K., Lee, D., Lumley, M. A. & Choi, K.-S. Progress on ternary oxide-based photoanodes for use in photoelectrochemical cells for solar water splitting. *Chem. Soc. Rev.* **48**, 2126–2157 (2019).
- Shi, X. B., Wu, Q. B. & Cui, C. H. Improving WO₃/SnO₂ photoanode stability by inhibiting hydroxyl radicals with cobalt ions in strong acid. *Sci. China Mater.* **66**, 614–622 (2023).
- Xie, M. F. et al. The role of titanium at the interface of hematite photoanode in multisite mechanism: Reactive site or cocatalyst site? *Chin. J. Catal.* **64**, 77–86 (2024).
- Kim, J. H., Hansora, D., Sharma, P., Jang, J.-W. & Lee, J. S. Toward practical solar hydrogen production - an artificial photosynthetic leaf-to-farm challenge. *Chem. Soc. Rev.* **48**, 1908–1971 (2019).
- Higashi, T. et al. Transparent Ta₃N₅ photoanodes for efficient oxygen evolution toward the development of tandem cells. *Angew. Chem. Int. Ed.* **58**, 2300–2304 (2019).
- Wang, L. et al. Dual effects of nanostructuring and oxygen vacancy on photoelectrochemical water oxidation activity of superstructured and defective hematite nanorods. *Small* **14**, 1704464 (2018).
- Wang, S. C., Liu, G. & Wang, L. Z. Crystal facet engineering of photoelectrodes for photoelectrochemical water splitting. *Chem. Rev.* **119**, 5192–5247 (2019).
- Ye, S. et al. Unassisted photoelectrochemical cell with multi-mediator modulation for solar water splitting exceeding 4% solar-to-hydrogen efficiency. *J. Am. Chem. Soc.* **143**, 12499–12508 (2021).
- Seitz, L. C. et al. Modeling practical performance limits of photoelectrochemical water splitting based on the current state of materials research. *ChemSusChem* **7**, 1372–1385 (2014).
- Zhao, S. X. et al. Sputtered stainless steel on silicon photoanode for stable seawater splitting in photoelectrochemical flow cell. *Trans. Tianjin Univ.* **29**, 473–481 (2023).
- Hoang, S., Guo, S. W., Hahn, N. T., Bard, A. J. & Mullins, C. B. Visible light driven photoelectrochemical water oxidation on nitrogen-modified TiO₂ nanowires. *Nano Lett.* **12**, 26–32 (2012).
- Wang, G. M. et al. Hydrogen-treated TiO₂ nanowire arrays for photoelectrochemical water splitting. *Nano Lett.* **11**, 3026–3033 (2011).
- Wang, G. M. et al. Hydrogen-treated WO₃ nanoflakes show enhanced photostability. *Energy Environ. Sci.* **5**, 6180–6187 (2012).
- Zhang, J. J. et al. WO₃ photoanodes with controllable bulk and surface oxygen vacancies for photoelectrochemical water oxidation. *J. Mater. Chem. A* **6**, 3350–3354 (2018).
- Lin, Y. J., Yuan, G. B., Sheehan, S., Zhou, S. & Wang, D. W. Hematite-based solar water splitting: challenges and opportunities. *Energy Environ. Sci.* **4**, 4862–4869 (2011).
- Zhang, Z. Z., Huang, X. J., Zhang, B. B. & Bi, Y. P. High-performance and stable BiVO₄ photoanodes for solar water splitting via phosphorus-oxygen bonded FeNi catalysts. *Energy Environ. Sci.* **15**, 2867–2873 (2022).
- Liu, B. Y. et al. A BiVO₄ photoanode with a VO_x layer bearing oxygen vacancies offers improved charge transfer and oxygen evolution kinetics in photoelectrochemical water splitting. *Angew. Chem. Int. Ed.* **62**, e202217346 (2023).
- Kim, J. H. et al. Hetero-type dual photoanodes for unbiased solar water splitting with extended light harvesting. *Nat. Commun.* **7**, 13380 (2016).
- Gong, Z. C. et al. Performance prediction of multiple photoanodes systems for unbiased photoelectrochemical water splitting. *ACS Mater. Lett.* **3**, 939–946 (2023).
- Sivula, K., Florian, L. F. & Grätzel, M. WO₃-Fe₂O₃ photoanodes for water splitting: a host scaffold guest absorber approach. *Chem. Mater.* **21**, 2862–2867 (2009).
- Liu, Y. et al. Efficient BiVO₄ photoanode with an excellent hole transport layer of CuSCN for solar water oxidation. *Adv. Energy Mater.* **14**, 2304223 (2024).
- Lin, Y. J., Zhou, S., Sheehan, S. W. & Wang, D. W. Nanonet-based hematite heteronanostructures for efficient solar water splitting. *J. Am. Chem. Soc.* **133**, 2398–2401 (2011).
- Gan, L., He, G. S., Liu, Y., Li, W. Z. & Li, J. Engineering heteropolyblue hole transfer layer for efficient photoelectrochemical water splitting of BiVO₄ photoanodes. *Appl. Catal. B* **349**, 123895 (2024).
- Li, H. M. et al. Controllable distribution of oxygen vacancies in grain boundaries of p-Si/TiO₂ heterojunction photocathodes for solar water splitting. *Angew. Chem. Int. Ed.* **60**, 4034–4037 (2021).
- Lu, J. T. et al. Strain engineering coupled with optical regulation towards a high-sensitivity In₂S₃ photodetector. *Mater. Horiz.* **7**, 1427–1435 (2020).
- Herzog, C., Belaidi, A., Ogacho, A. & Dittrich, T. Inorganic solid state solar cell with ultra-thin nanocomposite absorber based on nanoporous TiO₂ and In₂S₃. *Energy Environ. Sci.* **2**, 962–964 (2009).
- Chai, H. et al. In₂S₃/F-Fe₂O₃ type-II heterojunction bonded by interfacial S-O for enhanced charge separation and transport in photoelectrochemical water oxidation. *Appl. Catal. B* **305**, 121011 (2022).
- Zhang, J. J. et al. Tailored indium sulfide-based materials for solar-energy conversion and utilization. *J. Photochem. Photobiol. C. Photochem. Rev.* **38**, 1–26 (2019).
- Wu, R., Xu, Y., Xu, R., Huang, Y. & Zhang, B. Ultrathin-nanosheet-based 3D hierarchical porous In₂S₃ microspheres: chemical transformation synthesis, characterization, and enhanced photocatalytic and photoelectrochemical property. *J. Mater. Chem. A* **3**, 1930–1934 (2015).
- Jin, L., Wu, Y., Zhang, H. J. & Wang, Y. In-situ synthesis of the thinnest In₂Se₃/In₂S₃/In₂Se₃ sandwich-like heterojunction for photoelectrocatalytic water splitting. *Chem. Eur. J.* **28**, e202104428 (2022).
- Cao, S. Y. et al. 3D porous pyramid heterostructure array realizing efficient photo-electrochemical performance. *Adv. Energy Mater.* **10**, 1902935 (2020).
- Hou, J. G. et al. Atomically thin mesoporous In₂O_{3-x}/In₂S₃ lateral heterostructures enabling robust broadband-light photo-electrochemical water splitting. *Adv. Energy Mater.* **8**, 1701114 (2018).

39. Tian, W. et al. PVP treatment induced gradient oxygen doping in In_2S_3 nanosheet to boost solar water oxidation of WO_3 nanoarray photoanode. *Adv. Energy Mater.* **10**, 1903951 (2020).
40. Geng, H. M., Ying, P. Z., Li, K., Zhao, Y. L. & Gu, X. Q. Epitaxial $\text{In}_2\text{S}_3/\text{ZnIn}_2\text{S}_4$ heterojunction nanosheet arrays on FTO substrates for photoelectrochemical water splitting. *Appl. Surf. Sci.* **563**, 150289 (2021).
41. Yang, W., Prabhakar, R., Tan, R., Tilley, J. & Moon, S. D. J. Strategies for enhancing the photocurrent, photovoltage, and stability of photoelectrodes for photoelectrochemical water splitting. *Chem. Soc. Rev.* **48**, 4979–5015 (2019).
42. Abdi, F. F. et al. Efficient solar water splitting by enhanced charge separation in a bismuth vanadate-silicon tandem photoelectrode. *Nat. Commun.* **4**, 2195–2202 (2013).
43. Pan, L. F. et al. Boosting the performance of Cu_2O photocathodes for unassisted solar water splitting devices. *Nat. Catal.* **1**, 412–420 (2018).
44. Nayak, P. K., Mahesh, S., Snaith, H. J. & Cahen, D. Photovoltaic solar cell technologies: analysing the state of the art. *Nat. Rev. Mater.* **4**, 269–285 (2019).
45. Burst, J. M. et al. CdTe solar cells with open-circuit voltage breaking the 1V barrier. *Nat. Energy* **1**, 16015 (2016).
46. Ohashi, K., McCann, J. & Bockris, J. Stable photoelectrochemical cells for the splitting of water. *Nature* **266**, 610–611 (1977).
47. Lichterman, M. F. et al. Stabilization of n-cadmium telluride photoanodes for water oxidation to $\text{O}_2(\text{g})$ in aqueous alkaline electrolytes using amorphous TiO_2 films formed by atomic-layer deposition. *Energy Environ. Sci.* **7**, 3334–3337 (2014).
48. Kumar, S. G. & Rao, K. S. R. K. Physics and chemistry of CdTe/CdS thin film heterojunction photovoltaic devices: fundamental and critical aspects. *Energy Environ. Sci.* **7**, 45–102 (2014).
49. Chen, X. Y., Shen, X., Shen, S. H., Reese, M. O. & Hu, S. Stable CdTe photoanodes with energetics matching those of a coating intermediate band. *ACS Energy Lett.* **5**, 1865–1871 (2020).
50. Zhang, Y. T. et al. Simultaneously efficient solar light harvesting and charge transfer of hollow octahedral $\text{Cu}_2\text{S}/\text{CdS}$ p-n heterostructures for remarkable photocatalytic hydrogen generation. *Trans. Tianjin Univ.* **27**, 348–357 (2021).
51. Andrei, V. et al. Scalable triple cation mixed halide perovskite- BiVO_4 tandems for bias-free water splitting. *Adv. Energy Mater.* **8**, 1801403 (2018).
52. Jiang, F., Choy, W. C. H., Li, X. C., Zhang, D. & Cheng, J. Q. Post-treatment-free solution-processed non-stoichiometric NiO_x nanoparticles for efficient hole-transport layers of organic optoelectronic devices. *Adv. Mater.* **27**, 2930–2937 (2015).
53. Abzieher, T. et al. Electron-beam-evaporated nickel oxide hole transport layers for perovskite-based photovoltaics. *Adv. Energy Mater.* **9**, 1802995 (2019).
54. Boyd, C. C. et al. Overcoming redox reactions at perovskite-nickel oxide interfaces to boost voltages in perovskite solar cells. *Joule* **4**, 1759–1775 (2020).
55. Jeong, M. J. et al. Oxide/halide/oxide architecture for high performance semi-transparent perovskite solar cells. *Adv. Energy Mater.* **12**, 2200661 (2022).
56. Tan, J. W. et al. Fullerene as a photoelectron transfer promoter enabling stable TiO_2 -protected Sb_2Se_3 photocathodes for photoelectrochemical water splitting. *Adv. Energy Mater.* **9**, 1900179 (2019).
57. Bae, D., Seger, B., Vesborg, P. C. K., Hansen, O. & Chorkendorff, I. Strategies for stable water splitting via protected photoelectrodes. *Chem. Soc. Rev.* **46**, 1933–1954 (2017).
58. Chen, M. X. et al. Spatial control of cocatalysts and elimination of interfacial defects towards efficient and robust CIGS photocathodes for solar water splitting. *Energy Environ. Sci.* **11**, 2025–2034 (2018).
59. Chen, Y. W. et al. Atomic layer-deposited tunnel oxide stabilizes silicon photoanodes for water oxidation. *Nat. Mater.* **10**, 539–544 (2011).
60. Hu, S. et al. Amorphous TiO_2 coatings stabilize Si, GaAs, and GaP photoanodes for efficient water oxidation. *Science* **344**, 1005–1009 (2014).
61. Gu, J. et al. Water reduction by a p-GaInP₂ photoelectrode stabilized by an amorphous TiO_2 coating and a molecular cobalt catalyst. *Nat. Mater.* **15**, 456–460 (2016).
62. Digdaya, I. A. et al. Extracting large photovoltages from a-SiC photocathodes with an amorphous TiO_2 front surface field layer for solar hydrogen evolution. *Energy Environ. Sci.* **8**, 1585–1593 (2015).
63. Tang, C. G. et al. Doped polymer semiconductors with ultrahigh and ultralow work functions for ohmic contacts. *Nature* **539**, 536–540 (2016).
64. Lang, Q. Q. et al. Graphene “bridge” in transferring hot electrons from plasmonic Ag nanocubes to TiO_2 nanosheets for enhanced visible light photocatalytic hydrogen evolution. *Appl. Catal. B* **220**, 182–190 (2018).
65. Zhang, T. et al. Rationally designing high-performance versatile organic memristors through molecule-mediated ion movements. *Adv. Mater.* **35**, 2302863 (2023).
66. Park, J. et al. Hydrothermally obtained type-II heterojunction nanostructures of $\text{In}_2\text{S}_3/\text{TiO}_2$ for remarkably enhanced photoelectrochemical water splitting. *Appl. Catal. B* **295**, 120276 (2021).
67. Zhang, H. et al. Efficient and stable photoelectrochemical hydrogen generation using optimized colloidal heterostructured quantum dots. *Nano Energy* **79**, 105416 (2021).
68. Du, D. X. et al. One-step synthesis of aqueous CdTe/CdSe composite QDs toward efficiency enhancement of solar cell. *Chem. Eng. J.* **461**, 142040 (2023).
69. Bajorowicz, B., Nadolna, J., Lisowski, W., Klimczuk, T. & Zaleska-Medynska, A. The effects of bifunctional linker and reflux time on the surface properties and photocatalytic activity of CdTe quantum dots decorated KTaO_3 composite photocatalysts. *Appl. Catal. B* **203**, 452–464 (2017).
70. Chen, H.-C. et al. Enhanced performance and air stability of 3.2% hybrid solar cells: how the functional polymer and CdTe nanostructure boost the solar cell efficiency. *Adv. Mater.* **23**, 5451–5455 (2011).
71. Yang, P. & Murase, N. Preparation-condition dependence of hybrid SiO_2 -coated CdTe nanocrystals with intense and tunable photoluminescence. *Adv. Funct. Mater.* **20**, 1258–1265 (2010).
72. Pandya, R. et al. Exciton-phonon interactions govern charge-transfer-state dynamics in CdSe/CdTe two-dimensional colloidal heterostructures. *J. Am. Chem. Soc.* **140**, 14097–14111 (2018).
73. Li, Y. C. et al. High-yield fabrication and electrochemical characterization of tetrapodal CdSe, CdTe, and $\text{CdSe}_x\text{Te}_{1-x}$ nanocrystals. *Adv. Funct. Mater.* **16**, 1705–1716 (2006).
74. Paracchino, A. et al. Ultrathin films on copper(I) oxide water splitting photocathodes: a study on performance and stability. *Energy Environ. Sci.* **5**, 8673–8681 (2012).

Acknowledgements

The authors acknowledge the National Key R&D Program of China (2021YFA1500804 and 2022YFA1505200), the National Natural Science Foundation of China (22121004, 22038009 and 22250008), Haihe Laboratory of Sustainable Chemical Transformations (CYZC202107), the Program of Introducing Talents of Discipline to Universities (No. BP0618007) and the Xplorer Prize for financial support.

Author contributions

J.L.G. and T.W. designed and directed the research. J.L.G., T.W. and Y.C. conceptualized the project. Y.C. prepared a semi-transparent $\text{Ag}/\text{Ag}:\text{In}_2\text{S}_3/\text{In}_2\text{S}_3/\text{CdTe}/\text{NiO}_x/\text{TiO}_2/\text{Ni}$ photoanode and carried out the experiments and data analysis. S.J.W. and B.L. prepared the back-illuminated Si photocathodes and measured their performance. G.Z., H.G., Y.T.T. and Q.F.C. conducted long-term stability testing together.

P.Z. helps interpretation of the data. All authors participated in writing and revising the paper.

Competing interests

The authors declare no competing interests.

Additional information

Supplementary information The online version contains supplementary material available at <https://doi.org/10.1038/s41467-025-60444-7>.

Correspondence and requests for materials should be addressed to Tuo Wang or Jinlong Gong.

Peer review information *Nature Communications* thanks Zhiliang Wang and the other anonymous reviewer(s) for their contribution to the peer review of this work. A peer review file is available.

Reprints and permissions information is available at <http://www.nature.com/reprints>

Publisher's note Springer Nature remains neutral with regard to jurisdictional claims in published maps and institutional affiliations.

Open Access This article is licensed under a Creative Commons Attribution-NonCommercial-NoDerivatives 4.0 International License, which permits any non-commercial use, sharing, distribution and reproduction in any medium or format, as long as you give appropriate credit to the original author(s) and the source, provide a link to the Creative Commons licence, and indicate if you modified the licensed material. You do not have permission under this licence to share adapted material derived from this article or parts of it. The images or other third party material in this article are included in the article's Creative Commons licence, unless indicated otherwise in a credit line to the material. If material is not included in the article's Creative Commons licence and your intended use is not permitted by statutory regulation or exceeds the permitted use, you will need to obtain permission directly from the copyright holder. To view a copy of this licence, visit <http://creativecommons.org/licenses/by-nc-nd/4.0/>.

© The Author(s) 2025